nature physics

Article

https://doi.org/10.1038/s41567-023-02158-5

Trap-assisted formation of atom–ion bound states

Received: 21 August 2022

Accepted: 29 June 2023

Published online: 10 August 2023

Check for updates

Meirav Pinkas[1] ✉, Or Katz[1,2], Jonathan Wengrowicz[1], Nitzan Akerman[1] & Roee Ozeri[1] ✉

Pairs of free particles cannot form bound states in an elastic collision due to momentum and energy conservation. In many ultracold experiments, however, the particles collide in the presence of an external trapping potential that can couple their centre-of-mass and relative motions, assisting the formation of bound states. Here we report the observation of weakly bound molecular states formed between one ultracold atom and a single trapped ion in the presence of a linear Paul trap. We show that bound states can efficiently form in binary collisions, and enhance the rate of inelastic processes. By measuring the electronic spin-exchange rate, we study the dependence of these bound states on the collision energy and magnetic field, and extract the average molecular binding energy and mean lifetime of the molecule, having good agreement with molecular dynamics simulations. Our simulations predict a power-law distribution of molecular lifetimes with a mean that is dominated by extreme, long-lived events. The dependence of the molecular properties on the trapping parameters enables further studies on the characterization and control of ultracold collisions.

Collisions between pairs of particles are among the fundamental building blocks of molecular formation and quantum chemistry. Owing to energy and momentum conservation, pairs of free particles cannot bind in binary elastic collisions; instead, molecules' formation usually requires inelastic dynamics or three-body interactions, as realized in processes such as photoassociation[1–4], Feshbach association[5–8] or three-body recombination[9–11].

In many ultracold collision experiments, however, the particles are not free but trapped by an external potential, such as optical dipole traps[12–16] or ion traps[8,10,17–22]. Charged particles, in particular, are highly susceptible to electric fields and usually require strong electromagnetic potentials to assist trapping. In most trapped ion experiments, the ions are held in a Paul trap, using time-dependent electric fields[23,24].

Various studies have shown that the presence of a trap can modify the properties of collisions and lead to the emergence of unique phases[25,26], to change in the profile of scattering resonances[26–30], to non-equilibrium dynamics[31,32] or to the formation of bound states via the adiabatic merging of two different traps[33–35]. Yet, to date, trap-assisted bound states between pairs of neutral atoms and atomic ions have not been observed.

Here we show that the ion's confinement can lead to a short-lived and loosely bound $^{88}Sr^{+}$–^{87}Rb molecule in a cold binary collision. By measuring the probability of electronic spin exchange (SE) between the atom and ion at different settings, we estimate the molecule's lifetime and binding energy. We compare our results with a molecular dynamics (MD) simulation and characterize the trap effect for various experimental configurations. We show that the molecular lifetime is power-law distributed such that the mean molecular lifetime is dominated by extreme, long-lived events.

Formation and detection of atom–ion bound states

In most hybrid atom–ion experiments in the ultracold regime, both neutral atom and ion are trapped by external potentials. Yet, the dynamics is predominantly governed by the ion's trapping potential owing to its considerably high trapping frequency. This potential breaks the

[1]Department of Physics of Complex Systems and AMOS, Weizmann Institute of Science, Rehovot, Israel. [2]Present address: Duke Quantum Center, Department of Physics and Electrical and Computer Engineering, Duke University, Durham, NC, USA. ✉e-mail: meirav.pinkas@weizmann.ac.il; roee.ozeri@weizmann.ac.il

https://doi.org/10.1038/s41567-023-02158-5

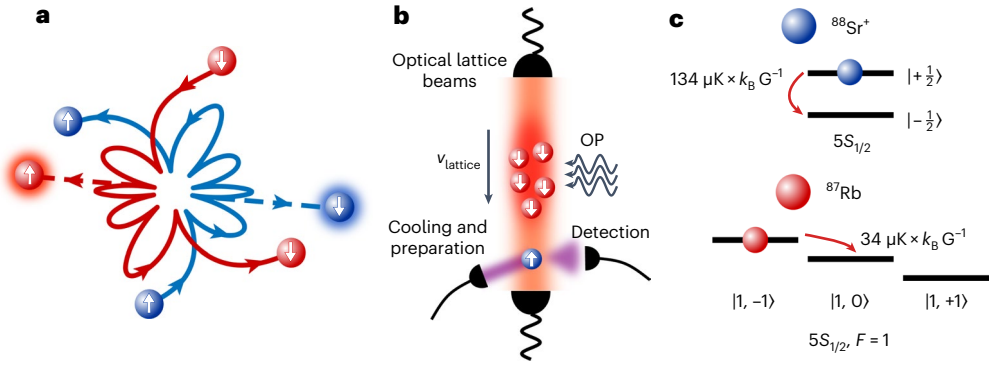

Fig. 1 | Bound state formation and experimental apparatus. a, Collision between an atom and an ion in the centre-of-mass frame when the ion is trapped in a harmonic trap. A bound state with five short-range collisions is formed (solid lines). If an exothermic SE occurs (a schematic for the second collision is shown here), the energy is released and the bound state may dissociate (dashed lines). **b**, Experimental setup. A cloud of Rb atoms is trapped, cooled down and loaded into an optical lattice trap. The atoms are optically pumped (OP) into a specific spin state. The atomic cloud is transported over the ion at velocity $v_{lattice}$. The ion is prepared in a specific spin state before the passage of the cloud, and typically a single Langevin collision occurs. Ion-state detection is realized afterwards using state-selective fluorescence. **c**, Energy levels for $^{88}Sr^+$ and ^{87}Rb in the electronic ground state. After the SE process (denoted by the red arrows for an exothermic process), the Zeeman energy is released or absorbed to the motional degrees of freedom.

translation-invariance symmetry of the interaction Hamiltonian and could hence generate a coupling between the relative motion and centre-of-mass motion of the atom–ion pair. This coupling could transfer energy between these two frames and reduce the pair's energy in the relative frame, consequently allowing short-lived bound states. A similar mechanism—inelastic confinement-induced resonance—leads to ultracold atoms to have bound states in anharmonic traps[36–39] or when the particles have different trapping frequencies[40].

We illustrate the bound-state formation (Fig. 1a) via the numerical simulation of a collision when an ideal, spherical symmetric harmonic potential is applied to the ion (Methods). Here the atom and ion bind in a binary collision; their relative motion manifests multiple oscillations, shown in the centre-of-mass frame. Consequently, during the lifetime of this molecule, the pair comes into close contact multiple times, enhancing the action of short-range chemical forces during the scattering, and increasing the probability of inelastic processes.

The total inelastic scattering rate depends on the elastic scattering rate and inelastic process probability. The number of distinct scattering events with different atoms is determined by the Langevin capture rate coefficient, $K_L = \pi\sqrt{4C_4/\mu}$ (ref. 3), where C_4 is the leading long-range induction coefficient of the interaction and μ is the reduced mass. In each Langevin collision, the atom and ion spiral towards each other, and have a single period of interaction if they remain free, or multiple periods of short-range interactions if a bound state is formed. Since chemical forces leading to inelastic scattering are short ranged, the inelastic process probability is primarily determined by the relative molecular potential curves at a scale of several Bohr radii[3,41]. On the other hand, two characteristic length scales are associated with the external trap. The first is the harmonic oscillator length, $r_{ho} \approx \sqrt{\hbar/m\omega}$, where m is the ion mass and ω is the trapping frequency. The second is the distance at which the polarization potential is equal to the ion's trapping potential, that is, $r \approx \sqrt[4]{C_4/m\omega^2}$ (ref. 42). Both length scales are about a few tens of nanometres and are considerably larger than the range of chemical forces. Owing to this length-scale separation, the inelastic short-range probability is unaffected by the trapping potential. Yet, bound states lead to multiple short-range encounters, and by that, enhance inelastic processes.

Experimental system

We study the formation of loosely bound ^{87}Rb–$^{88}Sr^+$ molecules using the experimental system (Fig. 1b) with the details provided elsewhere[32,43,44]. In brief, we trap and cool ^{87}Rb atoms in a magneto-optical trap (MOT) with a dark MOT stage followed by a polarization gradient cooling. A cloud of (5–10) × 10^5 atoms is loaded into a one-dimensional optical lattice created by two counterpropagating laser beams[44]. The atoms are optically pumped into one of the hyperfine states $|F = 1, m_F = \pm 1\rangle$ in the electronic ground state. The atomic cloud is transported through the Paul trap at a fixed velocity, equivalent to a kinetic energy of 100 μK, which is controlled by the optical frequency difference of the beams. A $^{88}Sr^+$ ion is trapped in a linear segmented Paul trap and is cooled using Doppler cooling, followed by resolved-sideband cooling into the ground state ($\bar{n} \lesssim 0.5$ in each motional mode). Then, the ion is optically pumped into one of the two Zeeman states of the electronic ground-state manifold $5S_{1/2}$. Following preparation and before overlapping with the atomic cloud, the magnetic field is changed from 3 G to a target value.

We measure the ion's spin state by double shelving one of the ground-state levels into two different Zeeman states in the $4D_{5/2}$ manifolds using a narrow-linewidth laser at 674 nm, followed by the detection of state-dependent fluorescence light using the strong $5S_{1/2}$–$5P_{1/2}$ dipole transition.

Enhancement of SE rate

SE is one of the most probable inelastic processes in $^{88}Sr^+$ and ^{87}Rb collisions[41,45]. In Fig. 1c, we illustrate an SE process between $^{88}Sr^+$ and ^{87}Rb in their electronic ground state. In the presence of a magnetic field, the SE is accompanied by an exchange of internal and kinetic energies. The SE rate was studied for exothermic and endothermic processes when the particles' initial states were $|\uparrow\rangle_{Sr^+}|1, -1\rangle_{Rb}$ and $|\downarrow\rangle_{Sr^+}|1, +1\rangle_{Rb}$, respectively. The energy gap for these two pathways depends on the magnetic field as $\Delta_{SE} = \pm h \times 3.5\ \text{MHz G}^{-1} = \pm 168\ \mu\text{K} \times k_B\ \text{G}^{-1}$, where h is Planck's constant and k_B is Boltzmann's constant.

In the experiment, the mean number of Langevin capturing events per passage of the atomic cloud through the ion trap is given by $N_L = \rho K_L / v_{lattice}$ (Methods and ref. 44), where ρ is the atomic column density of the neutral atoms integrated along the lattice direction of motion and $v_{lattice}$ is the speed of the lattice. The Langevin capture rate coefficient K_L is nearly independent of the collision energy or the magnetic field. All the experiments are taken at a constant lattice velocity, and therefore, the probability for at least one Langevin collision is constant and equal to 0.32(3) (Methods).

Energy dependence

We first study the dependence of SE on the ions' excess micromotion (EMM) energy E_{EMM}, which is the energy in the fast oscillatory motion in the frequency of the trapping radio-frequency (RF) fields. E_{EMM} is

https://doi.org/10.1038/s41567-023-02158-5

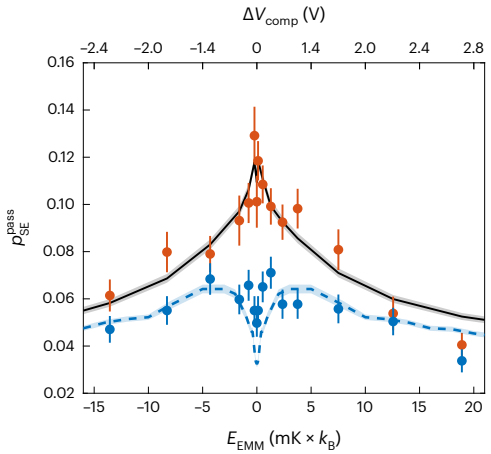

Fig. 2 | SE as a function of collision energy. SE probability per passage as a function of EMM energy is measured at 16 G for exothermic (red) and endothermic (blue) channels. The error bars are binomial-distribution standard deviation. Each point is an average of ~1,000 experiments. The black solid line is the maximum likelihood fit of the short-range SE probability based on a numerical simulation, including detection efficiency change due to heating (Methods), giving a probability of $p_{SE}^{0} = 0.122(4)$. The shaded area is the 1σ confidence bounds of the fit. The dashed blue line is the effective SE given by the simulation for the endothermic channel at $B = 16$ G transition when the short-range probability is 0.12, including detection efficiency.

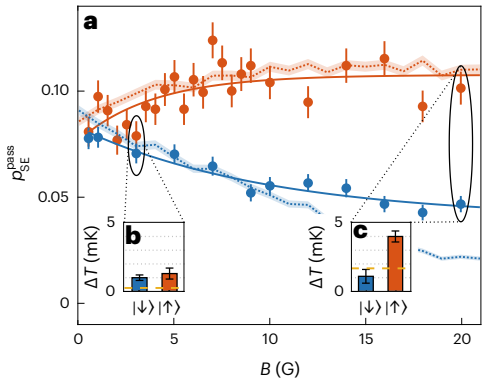

Fig. 3 | SE as a function of magnetic field and thermometry. a, SE probability per passage as a function of the magnetic field for the exothermic (red) and endothermic (blue) channels at a lattice velocity of 0.14 mm ms^{-1} (equivalent to 100 μK). The error bars are binomial-distribution standard deviation. Each point is an average of 1,500–3,000 experiments. The solid lines are the maximum likelihood estimation fit to a decay exponential function $p_{SE}^{pass} = A \times \exp(-B/B_0) + C$ for both experiments. The parameters are $A = -0.031(4)$, $B_0 = 3.9(7)$ G and $C = 0.108(2)$ for the exothermic channel and $A = 0.043(3)$, $B_0 = 10.0(1)$ G and $C = 0.040(1)$ for the endothermic channel. The dashed lines are the expected p_{SE}^{pass} values for the exothermic (red) and endothermic channels (blue) from the MD simulation, assuming the short-range $p_{SE}^{0} = 0.12$ that was found using the data shown in Fig. 2 with no fit parameters (Methods). **b**,**c**, Heating of the ion using Rabi carrier thermometry on the SE event of the two transitions at 3 G (**b**) and 20 G (**c**). The dashed yellow line denotes half of the Zeeman-gap energy.

determined by the voltage difference ΔV_{comp}, which is the difference between the voltage applied on one of the trap electrodes and the compensated voltage (Methods). In Fig. 2, we show the dependence of the measured SE probability per atomic cloud passage, p_{SE}^{pass}, on the micromotion energy at a background field of $B = 16$ G.

Although in the absence of a bound state, we expect p_{SE}^{pass} to be independent of the micromotion energy, our measurement shows exothermic channel enhancement at small E_{EMM}. The low-energy SE enhancement indicates the formation of a bound state, which leads to multiple short-range collisions.

At low micromotion energy, the endothermic SE is suppressed compared with the exothermic channel. This is expected since the kinetic energy of the bodies and the work done by the trap are smaller than the magnetic energy gap. However, at 16 G, the energy gap for an endothermic transition is about 2.5 mK, larger than all the other initial energy scales in the system. The lack of the complete suppression of endothermic SE is another indication of trap-associated effects, which could be explained by multiple short-range collisions during which work can be done by the trap time-dependent fields.

Magnetic-field dependence

We next turned to measure the SE dynamics at various magnetic fields. Owing to the conversion between internal magnetic energy and kinetic energy, we expect to see the enhancement or suppression of SE as a function of the magnetic field for different scattering pathways if a bound state is formed. The measured endothermic (exothermic) SE probability as a function of the magnetic field is shown by the blue (red) filled circles (Fig. 3).

The dependence of the exothermic channel on the magnetic field can be understood from its effect on the bound state's dissociation. At high magnetic fields, the released energy is larger than the binding energy. As a result, the bound state dissociates after the first SE event. At low magnetic fields, however, the ion's spin can flip multiple times in subsequent short-range encounters, which decreases the observed SE probability.

For the endothermic channel, SE still occurs in the highest measured magnetic field, despite the fact that it should be suppressed by energy conservation. We further characterized the dynamics by measuring the temperature of the ion, post-selected on experiments in which its spin had flipped. The measured temperatures are shown in Fig. 3b,c, using the Rabi carrier thermometry technique[20]. A reference temperature of non-SE events was separately measured for each channel (Methods). At a magnetic field of 3 G, both exothermic (red) and endothermic (blue) pathways leave the ion at a similar temperature, of about 1 mK, which is probably dominated by heating driven by the fields of the Paul trap[20,42]. At the highest magnetic field, after an exothermic transition, the ion heats up to a temperature comparable with the Zeeman gap. Surprisingly, after an endothermic transition, the temperature of the ion is similar to that measured at the low magnetic field, without any observed kinetic energy reduction, which is naively expected by the Zeeman-energy barrier. This might indicate additional trap-induced effects in this regime.

MD simulations

We compared our observations with an MD model, numerically simulating the dynamics of the collisions in a Paul trap (Methods). Using the simulation, we can study the distribution of the number of short-range collisions N. We find that for our experimental trapping parameters, a bound state is typically formed in a Langevin collision when EMM is compensated (Fig. 4a, blue line). In addition, the tail of the distribution exhibits a power-law behaviour, which scales roughly as $1/N^2$. For this distribution, the mean number of short-range collisions and the mean molecular lifetime are dominated by rare tail events. The power-law tail of the distribution is suppressed at higher micromotion energies, for example, at $E_{EMM} = 10$ mK k_B (Fig. 4a, red line).

When the collision energy is increased beyond the bound state's binding energy, the probability for more than one short-range collision p_{bound} is reduced (Fig. 4b). This coincides with the observed reduced SE probability at larger EMM (Fig. 2). However, bound states still occur for high values of EMM energies. Since the collision energy depends on the momentary phase of the RF field, low-energy events are still possible.

By fitting the exothermic SE probability in Fig. 2 to the numerical simulation results, we can extract the microscopic SE probability for a

https://doi.org/10.1038/s41567-023-02158-5

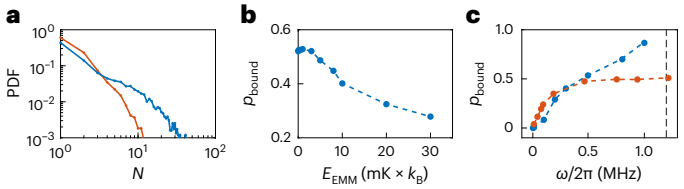

Fig. 4 | Bound-state properties from MD simulation. a, Probability density function (PDF) of the number of short-range collisions between the Sr^+ and Rb pair when the EMM is compensated (blue), and equivalent to 10 mK k_B (red). **b**, Bound-state probability, in a single Langevin collision, as a function of EMM energy, for the experimental parameters. **c**, Bound-state probability in a single Langevin collision in a harmonic trap (blue) and a Paul trap (red) as a function of trap frequency. The harmonic trap is a spherical symmetric trap with frequency ω. The Paul trap is a linear trap with an axial trapping frequency $\omega_{ax} = 2\pi \times 3.00$ kHz, RF driving frequency $\Omega_{RF} = 2\pi \times 26.51$ MHz and secular radial trapping frequency ω, for an ion with zero initial energy. The black dashed line denotes the mean radial frequency in the experiment. In all the graphs, the magnetic field is zero, and the Rb atoms have a velocity equivalent to 100 μK. The binomial confidence bounds of 1σ are smaller than the marker size.

single short-range interaction, giving $p^0_{SE} = 0.122(4)$ (Methods) (Fig. 2, black line). This probability is consistent with previous measurements at higher energies[46]. The dashed blue line in this figure shows the predictions of our model for the endothermic channel given $p^0_{SE} = 0.12$. Evidently, our model predicts a much stronger suppression at low energy than measured.

Using the estimated p^0_{SE}, we can find—using the MD simulation—the expected p^{pass}_{SE} value as a function of the magnetic field (Fig. 3, dotted lines) with no other fit parameters. The simulation results agree with the enhancement in exothermic SE as a function of the magnetic field, and the suppression of the endothermic SE in the low-magnetic-field regime. The MD simulations of the endothermic channel underestimate the SE probability at high magnetic fields compared with the measured data. This difference might result from effects not included in the simulation (Supplementary Note II).

The formation of trap-induced bound states is a universal phenomena that can emerge at different trap configurations. For example, in Fig. 4c, we show the bound-state probability p_{bound} as a function of the secular trap frequency ω for an ideal, time-independent spherical symmetric harmonic trap (blue) and a Paul trap (red) with radial frequency ω and fixed axial frequency. Evidently, a trap can lead to bound states in binary collisions. For the harmonic case, the bound-state probability increases with the trap frequency to close to unity, but saturates for a Paul trap at $p_{bound} \simeq 0.5$, owing to work done by the time-dependent fields that can prevent molecular binding[42]. The binding probability also depends on the atom–ion mass ratio (Extended Data Fig. 1b). For the harmonic case, the coupling term or the Hamiltonian is given by $H_{cpl} = \omega^2 \mu R \cdot r$, where μ is the reduced mass and r (R) is the relative (centre-of-mass) coordinate (Supplementary Note I). This coupling is negligible for a free ion, or smaller reduced mass, which is qualitatively reproduced in the simulation results.

Binding energy and lifetime of trapped-assisted bound states

We can use our measured data to estimate different parameters of the loosely bound molecules. The maximum likelihood estimation of the magnetic dependence of the exothermic channel to an exponential decay gives a decay constant of $B_0 = 3.9(7)$ G, corresponding to the mean bond energy of $E_{bind} = \Delta_{SE} B_0 = 0.7(1)$ mK. The likelihood of the exponential decay can be compared with a constant probability model using a likelihood ratio test, giving a p value of 1.2×10^{-5}. For comparison, in the bound state of neutral atoms due to inelastic confinement-induced resonance, the binding energy is on the order of a few harmonic oscillator quanta[36]. For our case, $E_{bind} \times k_B/h = 15(2)$ MHz is ~10 quanta of the secular frequency. However, the RF fields might play a role in setting the binding energy.

By a simple model for a bound state, the number of short-range collisions and the resulting molecular lifetime can be roughly estimated from the experiment, without a full calculation of the particles' trajectories (Methods). Using this model, we find the effect on the probability of SE in a single atomic cloud pass. The bound state can be modelled by assuming that the number of short-range interaction periods N has a geometric distribution with probability $1/\langle N \rangle$. For any short-range SE probability p^0_{SE}, we can calculate what would be the effective SE in the two regimes: when the process has no energetic gap (zero magnetic field) and when the process is exothermic with an energetic gap larger than the binding energy (large magnetic field) (Methods). This amplification depends on both p^0_{SE} and $\langle N \rangle$, and is extracted from the experiment using an exponential fit to the exothermic channel (Fig. 3). Combining both measured amplification and the estimation for p^0_{SE} and comparing the model, the mean number of collisions in the experiment is $\langle N \rangle^{exp} = 8(2)$ (Extended Data Fig. 2). Assuming the binding is only due to the $C_4/2r^4$ potential, the time between collisions is $T = 62$ ns (Methods), and we can estimate the lifetime of the molecule in the experiment as 0.5(1) μs, similar to the mean lifetime given by the MD simulation, namely, 0.411(4) μs.

Discussion

We have observed the formation of trap-assisted bound states in ultracold atom–ion collisions. These bound states amplify the rate of inelastic processes in both exothermic and endothermic collision channels. From the measured SE rates, we estimated the molecules' binding energy as 0.7(1) mK and mean lifetime as 0.5(1) μs.

Remarkably, bound states are efficiently formed in binary collisions. Numerical simulations indicate formation for every other collision and the molecular lifetime with a power-law distribution. Power laws in the energy distribution were already observed in atom–ion collisions due to multiplicative energy fluctuations after multiple collisions[20,31,32]. However, in this case, the power law arises in a single collision.

The trap parameters can control the molecular binding probability and lifetime, providing a convenient control knob. We observe that trap-assisted bound states are also efficiently formed in static potentials. This indicates that the source for binding is the coupling between the relative and centre-of-mass motion by breaking translational symmetry rather than the presence of time-dependent fields in Paul traps. Therefore, this effect can still play a role in atom–ion interactions using an optical trap for the ions[14].

These bound states introduce a systematic effect that potentially needs to be accounted for in analysing the scattering processes near the s-wave regime[34,47]. Yet, for a small atom–ion mass ratio $m_a \ll m_i$ and weak trapping frequencies, the formation of bound states is suppressed[48].

The formation of bound states by the trap is akin to the mechanism in which ultracold atoms can bind in anharmonic traps, related to inelastic confinement-induced resonances[36–39]. Yet, we expect the bound-state formation to qualitatively differ from the case of neutral atoms in two main aspects. First, because the external forces primarily trap the ion but not the atom, translational variance leads to efficient coupling between the centre-of-mass motion and relative motion (Supplementary Note I). For cold neutral atoms, on the other hand, owing to the nearly harmonic trapping potential, such formation is suppressed, and strong anharmonicity is required. Therefore, this effect might be pronounced in various hybrid atom–ion experiments. Second, the time-dependent trapping fields exert work on the ion that shortens the bound state's lifetime. We, therefore, expect that ultracold atoms or ions held in energy-conservative optical traps would feature longer bound-state lifetimes.

The formation of bound states can potentially enhance the probability of other inelastic processes or chemical reactions, as suggested recently[49]. Yet, owing to the coupling between the centre-of-mass and relative motion, energy from the centre-of-mass frame can potentially broaden the collision energy and hinder the observation of low-energy resonant processes, such as shape and Feshbach resonances.

Here we have explained our observations using classical simulations and did not include any quantum effects. In a quantum description, the trap might introduce a dense spectrum of resonances, similar to molecular 'sticky collisions'[50]. Moreover, the measured endothermic SE substantially deviates from the predictions of our simulations at a low collision energy and strong magnetic field. This could be, for example, due to the effect of multiple overlapping Feshbach resonances at these magnetic fields.

Online content

Any methods, additional references, Nature Portfolio reporting summaries, source data, extended data, supplementary information, acknowledgements, peer review information; details of author contributions and competing interests; and statements of data and code availability are available at https://doi.org/10.1038/s41567-023-02158-5.

References

1. Jones, K. M., Tiesinga, E., Lett, P. D. & Julienne, P. S. Ultracold photoassociation spectroscopy: long-range molecules and atomic scattering. *Rev. Mod. Phys.* **78**, 483–535 (2006).
2. Idziaszek, Z., Simoni, A., Calarco, T. & Julienne, P. S. Multichannel quantum-defect theory for ultracold atom–ion collisions. *New J. Phys.* **13**, 083005 (2011).
3. Tomza, M. et al. Cold hybrid ion-atom systems. *Rev. Mod. Phys.* **91**, 035001 (2019).
4. Jyothi, S. et al. Photodissociation of trapped Rb_2^+ implications for simultaneous trapping of atoms and molecular ions. *Phys. Rev. Lett.* **117**, 213002 (2016).
5. Köhler, T., Góral, K. & Julienne, P. S. Production of cold molecules via magnetically tunable Feshbach resonances. *Rev. Mod. Phys.* **78**, 1311–1361 (2006).
6. Chin, C., Grimm, R., Julienne, P. & Tiesinga, E. Feshbach resonances in ultracold gases. *Rev. Mod. Phys.* **82**, 1225–1286 (2010).
7. Drews, B., Deiß, M., Jachymski, K., Idziaszek, Z. & Denschlag, J. Hecker Inelastic collisions of ultracold triplet Rb_2 molecules in the rovibrational ground state. *Nat. Commun.* **8**, 14854 (2017).
8. Weckesser, P. et al. Observation of Feshbach resonances between a single ion and ultracold atoms. *Nature* **600**, 429–433 (2021).
9. Härter, A. et al. Single ion as a three-body reaction center in an ultracold atomic gas. *Phys. Rev. Lett.* **109**, 123201 (2012).
10. Mohammadi, A. et al. Life and death of a cold $BaRb^+$ molecule inside an ultracold cloud of Rb atoms. *Phys. Rev. Research* **3**, 013196 (2021).
11. Krükow, A. et al. Energy scaling of cold atom-atom-ion three-body recombination. *Phys. Rev. Lett.* **116**, 193201 (2016).
12. Grimm, R., Weidemuller, M. & Ovchinnikov, Y. B. *Optical Dipole Traps* Vol. 42 (Academic Press, 2000).
13. Anderegg, L. et al. An optical tweezer array of ultracold molecules. *Science* **365**, 1156–1158 (2019).
14. Lambrecht, A. et al. Long lifetimes and effective isolation of ions in optical and electrostatic traps. *Nat. Photon.* **11**, 704–707 (2017).
15. Reynolds, L. A. et al. Direct measurements of collisional dynamics in cold atom triads. *Phys. Rev. Lett.* **124**, 073401 (2020).
16. Schmidt, J., Weckesser, P., Thielemann, F., Schaetz, T. & Karpa, L. Optical traps for sympathetic cooling of ions with ultracold neutral atoms. *Phys. Rev. Lett.* **124**, 053402 (2020).
17. Grier, A. T., Cetina, M., Oručević, F. & Vuletić, V. Observation of cold collisions between trapped ions and trapped atoms. *Phys. Rev. Lett.* **102**, 223201 (2009).
18. Ratschbacher, L., Zipkes, C., Sias, C. & Köhl, M. Controlling chemical reactions of a single particle. *Nat. Phys.* **8**, 649–652 (2012).
19. Hall, F. H. J. & Willitsch, S. Millikelvin reactive collisions between sympathetically cooled molecular ions and laser-cooled atoms in an ion-atom hybrid trap. *Phys. Rev. Lett.* **109**, 233202 (2012).
20. Meir, Z. et al. Dynamics of a ground-state cooled ion colliding with ultracold atoms. *Phys. Rev. Lett.* **117**, 243401 (2016).
21. Saito, R. et al. Characterization of charge-exchange collisions between ultracold ^6Li atoms and $^{40}Ca^+$ ions. *Phys. Rev. A* **95**, 032709 (2017).
22. Joger, J. et al. Observation of collisions between cold Li atoms and Yb^+ ions. *Phys. Rev. A* **96**, 030703 (2017).
23. Paul, W. Electromagnetic traps for charged and neutral particles (Nobel Lecture). *Angew. Chem. Int. Ed.* **29**, 739–748 (1990).
24. Leibfried, D., Blatt, R., Monroe, C. & Wineland, D. Quantum dynamics of single trapped ions. *Rev. Mod. Phys.* **75**, 281–324 (2003).
25. Hadzibabic, Z., Krüger, P., Cheneau, M., Battelier, B. & Dalibard, J. Berezinskii-Kosterlitz-Thouless crossover in a trapped atomic gas. *Nature* **441**, 1118–1121 (2006).
26. Kinoshita, T., Wenger, T. & Weiss, D. S. Observation of a one-dimensional Tonks-Girardeau gas. *Science* **305**, 1125–1129 (2004).
27. Olshanii, M. Atomic scattering in the presence of an external confinement and a gas of impenetrable bosons. *Phys. Rev. Lett.* **81**, 938–941 (1998).
28. Mies, F. H., Tiesinga, E. & Julienne, P. S. Manipulation of Feshbach resonances in ultracold atomic collisions using time-dependent magnetic fields. *Phys. Rev. A* **61**, 022721 (2000).
29. Haller, E. et al. Confinement-induced resonances in low-dimensional quantum systems. *Phys. Rev. Lett.* **104**, 153203 (2010).
30. Kestner, J. P. & Duan, L. M. Anharmonicity-induced resonances for ultracold atoms and their detection. *New J. Phys.* **12**, 053016 (2010).
31. Rouse, I. & Willitsch, S. Superstatistical energy distributions of an ion in an ultracold buffer gas. *Phys. Rev. Lett.* **118**, 143401 (2017).
32. Meir, Z. et al. Direct observation of atom-ion nonequilibrium sympathetic cooling. *Phys. Rev. Lett.* **121**, 53402 (2018).
33. Stock, R., Ivan, H. D. & Bolda, E. L. Quantum state control via trap-induced shape resonance in ultracold atomic collisions. *Phys. Rev. Lett.* **91**, 183201 (2003).
34. Idziaszek, Z., Calarco, T. & Zoller, P. Controlled collisions of a single atom and an ion guided by movable trapping potentials. *Phys. Rev. A* **76**, 033409 (2007).
35. Melezhik, V. S. & Negretti, A. Confinement-induced resonances in ultracold atom-ion systems. *Phys. Rev. A* **94**, 022704 (2016).
36. Sala, S., Schneider, P. I. & Saenz, A. Inelastic confinement-induced resonances in low-dimensional quantum systems. *Phys. Rev. Lett.* **109**, 073201 (2012).
37. Sala, S. et al. Coherent molecule formation in anharmonic potentials near confinement-induced resonances. *Phys. Rev. Lett.* **110**, 203202 (2013).
38. Lee, Y. K., Lin, H. & Ketterle, W. Spin dynamics dominated by superexchange via virtual molecules. Preprint at *arXiv* https://arxiv.org/abs/2208.06054 (2022).
39. Capecchi, D. et al. Observation of confinement-induced resonances in a 3D lattice. Preprint at *arXiv* https://arxiv.org/abs/2209.12504 (2022).
40. Melezhik, V. S. & Schmelcher, P. Quantum dynamics of resonant molecule formation in waveguides. *New J. Phys.* **11**, 73031–73041 (2009).
41. Côté, R. & Dalgarno, A. Ultracold atom-ion collisions. *Phys. Rev. A* **62**, 012709 (2000).

42. Cetina, M., Grier, A. T. & Vuletić, V. Micromotion-induced limit to atom-ion sympathetic cooling in Paul traps. *Phys. Rev. Lett.* **109**, 253201 (2012).
43. Katz, O., Pinkas, M., Akerman, N. & Ozeri, R. Quantum logic detection of collisions between single atom-ion pairs. *Nat. Phys.* **18**, 533–537 (2022).
44. Ben-shlomi, R. et al. High-energy-resolution measurements of an ultracold-atom–ion collisional cross section. *Phys. Rev. A* **103**, 032805 (2021).
45. Aymar, M., Guérout, R. & Dulieu, O. Structure of the alkali-metal-atom strontium molecular ions: towards photoassociation and formation of cold molecular ions. *J. Chem. Phys.* **135**, 064305 (2011).
46. Sikorsky, T., Meir, Z., Ben-shlomi, R., Akerman, N. & Ozeri, R. Spin-controlled atom-ion chemistry. *Nat. Commun.* **9**, 920 (2018).
47. Katz, O., Pinkas, M., Akerman, N. & Ozeri, R., Quantum suppression of cold reactions far from the quantum regime. Preprint at *arXiv* https://arxiv.org/abs/2208.07725 (2022).
48. Feldker, T. et al. Buffer gas cooling of a trapped ion to the quantum regime. *Nat. Phys.* **16**, 413–416 (2020).
49. Hirzler, H., Trimby, E., Gerritsma, R., Safavi-Naini, A. & Pérez-Ríos, J. Trap-assisted complexes in cold atom-ion collisions. *Phys. Rev. Lett.* **130**, 143003 (2023).
50. Gregory, P. D. et al. Sticky collisions of ultracold RbCs molecules. *Nat. Commun.* **10**, 3104 (2019).

Methods

Experimental sequence

A cloud of ^{87}Rb atoms is trapped and cooled down using an MOT, followed by a dark MOT stage and a polarization gradient cooling. A cloud of ~10^6 atoms is loaded into an optical lattice created by counterpropagating 1,064 nm laser beams. The atoms are pumped into one of the hyperfine states, namely, $|1, -1\rangle$ or $|1, +1\rangle$, by a sequence of microwave and optical pulses. After pumping, more than 90% of the population is in the desired spin state.

The ion is trapped in a linear segmented Paul trap where the secular frequencies are $f = (1.10, 1.30, 0.48)$ MHz, and $\Omega_{RF} = 2\pi \times 26.51$ MHz. The ion is Doppler cooled and subsequently cooled near its ground state with $\bar{n} < 0.5$ in each of the motional modes. The atoms are moved to the lower chamber by changing the relative frequency between the lattice beams. Unless stated otherwise, the atoms are moved over the ion at a velocity of 0.14 m s^{-1}, which is equivalent to a kinetic energy of 100 μK. The current in the quantization coils is ramped up or down after cooling of the ion, and 30 ms before the collision. After the atomic cloud passes the ion, the magnetic field is ramped back to its initial value for state detection of the ion. Due to eddy currents in the system, the magnetic field has a transient time of 5 ms.

The spin-state detection was done 70 ms after the current in the quantization coils returned to its initial value and consists of two stages. First, we apply two π-pulses from the spin state that was not the initial state to two different states in the $D_{5/2}$ manifold (double shelving). For example, in the exothermic transition, the ion is initialized at $|+1/2\rangle$, the detection π-pulses are $|-1/2\rangle \rightarrow |-5/2\rangle$ and $|-1/2\rangle \rightarrow |+3/2\rangle$. After the shelving pulses, a fluorescence detection scheme is applied to check whether the ion spin was changed or not. If SE did not occur, the ion remains in the $S_{1/2}$ manifold and will appear bright. Otherwise, it is shelved into the $D_{5/2}$ manifold and no photons are detected. As a result of avoided crossing (Supplementary Note III), preparation and detection pulses are changed accordingly above 9.5 G.

The same detection scheme is applied for the same experimental sequence, but without atoms, to detect the preparation efficiency of the ion's spin state, which is independent of the magnetic field and EMM, and is about 0.5%. Experiments are taken interlacing over the scanned variables and the background experiments.

EMM is compensated every hour during the experiment to less than 50 μK for each of the radial modes and to a few microkelvins in the axial direction.

Measuring the probability of Langevin collisions

For two free particles, the Langevin rate is given by

$$\Gamma_L = n\sigma_L(E_{col})\sqrt{\frac{2E_{col}}{\mu}}, \tag{1}$$

where n is the atomic density, σ_L is the total Langevin cross section, E_{col} is the energy of the collision in the centre-of-mass frame and μ is the reduced mass. Classically, the cross section is given by $\sigma_L = \pi\sqrt{2C_4/E_{col}}$, and therefore, the reaction rate coefficient is

$$K_L = \sigma_L(E_{col})\sqrt{\frac{2E_{col}}{\mu}} = \pi\sqrt{\frac{4C_4}{\mu}}, \tag{2}$$

which is independent of the collision energy.

In the experiment, the atomic density in the ion position n is time dependent due to the movement of the lattice[44], and the number of Langevin collisions per passage is given by

$$N_L = K_L \int_{-\infty}^{\infty} n(t)\mathrm{d}t. \tag{3}$$

Assuming the lattice is moving in a constant velocity $v_{lattice}$, the number of collisions can be written as a function of the atomic density integrated along the direction of motion ρ as

$$N_L = \frac{K_L}{v_{lattice}} \int_{-\infty}^{\infty} n(x)\mathrm{d}x \equiv \frac{\rho K_L}{v_{lattice}}, \tag{4}$$

where x is the position of the ion relative to the centre of the atomic cloud.

We measured the number of collisions per passage by measuring the failure probability to shelve the ion from the electronic ground state to the D level using a long shelving pulse (14.6 μs) in the presence of high EMM energy ($E_{EMM} = 2.5$ K), as described elsewhere[47]. Under these conditions, a Langevin collision will efficiently couple the EMM energy to the secular motion[51] and consequently decrease the shelving probability. We numerically simulate this process[47], and find that the expected probability for a shelving failure per Langevin collision is about 87%.

We measure the shelving failure probability per passage of the cloud and present it (Extended Data Fig. 3) as the probability of observing the ion in a bright state after two shelving pulses as a function of the velocity of the ultracold atomic cloud. We find that the probability fits well to

$$p_{bright} = \rho K_L / v_{lattice} + p_{bg}, \tag{5}$$

where the first term is expected from equation (4), and the second term describes a constant background. From the maximum likelihood estimation, $\rho K_L = 0.039(3)$ and $p_{bg} = 0.078(8)$. The background probability is not due to finite shelving efficiency (which is 98.4(3)%), but probably due to hot atoms that are not trapped in the lattice. Taking into account the detection efficiency of a collision, at a collision energy of 100 μK, the probability for a cold Langevin collision in a single pass is $p_L^{lattice} = 0.32(3)$ with a background of about $p_L^{bg} = 0.089(4)$. This value corresponds to the probability to have at least one collision in a pass. Assuming the number of collisions in a single pass has a Poisson distribution, the mean number of collisions per pass is $\langle N \rangle = 0.385$, with a probability of $p_L^{single} = 0.26$ for a single collision and $p_L^{multiple} = 0.06$ for multiple collisions.

Rabi carrier thermometry

The temperature of the ion after a collision is measured by Rabi carrier thermometry[20,52]. The probability of observing the ion in the $D_{5/2}$ manifold after a resonant pulse driving the $S_{1/2} \rightarrow D_{5/2}$ transition with duration t is given by[24]

$$P_D(t) = \sum_{\mathbf{n}} P(\mathbf{n}) \sin^2(\Omega_{\mathbf{n},\mathbf{n}}), \tag{6}$$

where $P(\mathbf{n})$ is the occupation probability of the Fock state $\mathbf{n}$. Here $\Omega_{\mathbf{n},\mathbf{n}}$ is the coupling strength between $|S_{1/2}\rangle|\mathbf{n}\rangle$ and $|D_{5/2}\rangle|\mathbf{n}\rangle$ is given by[24]

$$\Omega_{\mathbf{n},\mathbf{n}} = \Omega_0 \prod_i \mathrm{e}^{\eta_i^2/2} L_{n_i}(\eta_i^2), \tag{7}$$

where Ω_0 is the scaled interaction strength, η_i is the Lamb–Dicke parameter of the ith mode and $L_n(x)$ is the nth Laguerre polynomial. The Fock states are assumed to be thermally distributed with a mean occupation number $\bar{\mathbf{n}}$:

$$P(\mathbf{n};\bar{\mathbf{n}}) = \prod_i \frac{1}{\bar{n}_i + 1}\left(\frac{\bar{n}_i}{\bar{n}_i + 1}\right)^{n_i}. \tag{8}$$

At higher temperatures, more values of n need to be considered in this distribution. At temperatures above 2 mK, we approximate the energy distribution by

$$P(E) = \frac{1}{(k_B T)^3} E^2 \mathrm{e}^{-\frac{E}{k_B T}}, \tag{9}$$

where $E = \sum_i \hbar\omega_i n_i$ and n_i is taken over a logarithmic scale. The contrast of a Rabi cycle post-selecting the spin state proportional to the SE probability is given by

$$P_D(t; p_{SE}) = p_{SE}^{pass} P_D(t). \tag{10}$$

The parameters T, Ω_0 and p_{SE}^{pass} are found by the maximum likelihood estimation of the experimental results to $P_D(t; p_{SE})$ assuming that the number of dark events follows a binomial distribution. The Rabi oscillations for the temperature measurements in Fig. 3b,c are shown in Extended Data Fig. 4.

EMM energy calibration

We control the EMM energy by changing the voltage difference ΔV_{comp} on an additional electrode, relative to the compensated value, generating a static electric field that shifts the equilibrium position of the ion away from the RF null of the Paul trap's potential. Consequently, the ion is subject to the trap's electric field in the radial direction that oscillated at Ω_{RF}, generating EMM displacements at the same frequency with amplitude $\mathbf{u}_{EMM}$. The EMM energy the ion gains is, therefore,

$$E_{EMM} = \frac{m_i (u_{EMM}\Omega_{RF})^2}{4}. \tag{11}$$

We measure the EMM oscillation amplitude as a function of ΔV_{comp} by following the protocol in other works[53,54], namely, by comparing Ω_0, the Rabi frequency of the carrier $S_{1/2}$–$D_{5/2}$ transition, with Ω_{sb}, the Rabi frequency of the first micromotion sideband transition (that is, a transition detuned from the carrier transition by micromotion frequency Ω_{RF}). The ratio of these two Rabi frequencies is related to u_{EMM} by

$$\frac{\Omega_{sb}}{\Omega_0} = \frac{\mathbf{k}\cdot\mathbf{u}_{EMM}}{2}, \tag{12}$$

where $\mathbf{k}$ is the wavevector of the narrow-linewidth laser at 674 nm that we used to drive the transition. Equation (12) holds for weak micromotion amplitudes $\mathbf{k}\cdot\mathbf{u}_{EMM} \ll 1$ (ref. 53), which is valid in our experiment.

We measure Ω_{sb} and Ω_0 as a function of ΔV_{comp} and show the projection of the micromotion amplitude along the optical axis $\hat{k}$ (Extended Data Fig. 5) using equation (12). We fit the data to the following function:

$$\mathbf{u}_{EMM}\cdot\hat{\mathbf{k}} = \sqrt{\gamma_{proj}^2 (V - V_0)^2 + c^2}, \tag{13}$$

where V is the applied voltage, V_0 is the value at which micromotion is compensated and $\Delta V_{comp} = V - V_0$. The coefficient γ_{proj}, offset c and V_0 are the fitting parameters of this model. We use parameter c because the estimation of Ω_{sb} is limited by the coherence time of the system[54]. However, the electrode's response is solely given by γ_{proj}. We find $\gamma_{proj} = 3.97(6)$ nm V^{-1}, $V_0 = -74.68(2)$ V and $c = 2.8(2)$ nm with 1σ confidence bounds. We extract the total micromotion amplitude by accounting for the relative orientation of $\hat{k}$ with respect to the trap axes. In our trap apparatus, $\hat{k} = \frac{1}{\sqrt{2}}(\hat{y} + \hat{z})$ and $\hat{u}_{EMM} = \cos(19°)\hat{y} + \sin(19°)\hat{x}$, as was previously measured in another work[54], using the trap coordinates $\hat{z}$ for the axial and $\hat{x}$, $\hat{y}$ for the radial directions. The geometric factor is, therefore, $\hat{k}\cdot\hat{u}_{EMM} = 0.667$. We can then calibrate the dependence of the EMM energy in equation (11) on the applied voltage in equation (13), yielding $E_{EMM}/\Delta V_{comp}^2 = 2.58$ mK V^{-2}.

MD simulation

Based on other work[32,42,52], we solve Newton's equations of motion for the atom and ion Hamiltonian:

$$H = \frac{\hat{\mathbf{p}}_i^2}{2m_i} + \frac{m_i\Omega_{RF}^2}{8}\sum_j \left[a_j + 2q_j\cos(\Omega_{RF}t)\right]\hat{r}_{i,j}^2 + \frac{\hat{\mathbf{p}}_a^2}{2m_a} + V(|\hat{\mathbf{r}}_i - \hat{\mathbf{r}}_a|), \tag{14}$$

where $m_{i(a)}$ is the ion (atom) mass, $r_{i(a),j}$ is the ion (atom) position in the jth direction, $V(|\hat{\mathbf{r}}_i - \hat{\mathbf{r}}_a|)$ is the atom–ion interaction potential, Ω_{RF} is the RF used and a_j and q_j are the trap parameters in the jth direction. Unless stated otherwise, $a = (-2.20, 0.83, 1.30)\times 10^{-3}$ and $q = (-0.134, 0.134, 0)$, reproducing the secular trapping frequencies of $f = (1.10, 1.30, 0.48)$ MHz, as in the experiment. We use the asymptotic form of the atom–ion interaction potential $V(r) = -2C_4/r^4$ at all distances larger than 10 nm, where the coefficient $C_4 = 1.09\times 10^{-56}$ J m^4 is predominantly determined by the neutral atom polarizability. The short-range atom–ion potential is modelled by an infinite wall at 10 nm. At this point, the particles collide in an elastic hard-sphere collision. Without SE, after the collisions, the velocities in the collision axis are changed assuming the conservation of momentum and energy in the centre-of-mass frame. Because the masses of ^{87}Rb and ^{88}Sr$^+$ are nearly equal, the velocities are nearly equal, too, but change their sign in the centre-of-mass frame.

The atoms start their trajectory on a plane 1.2 μm from the centre of the trap and the ion has an initial temperature of 150 μK (unless stated otherwise) divided equally in the different secular motional modes. The velocity distribution of the atoms consists of two terms, a thermal term ($T = 5$ μK) and a constant velocity that corresponds to the velocity of the optical lattice. For each set of parameters, the total number of calculated trajectories is 10^4, out of which about 40% have at least one short-range collision. The confidence bounds of the bound state and SE probabilities are 1σ of a binomial distribution.

The kinetic effect of an SE process is modelled by energy absorption or release after the hard-sphere collision. The probability of an SE to happen is calculated by the acceptance–rejection method, for the given p_{SE}^0 value. If SE occurred, the momentum and energy is no longer conserved. The momentum is altered only along the collision axis, and the ion's and atom's velocities parallel to the collision axis after the collision are updated by

$$u_i^{\parallel} = v_{cm}^{\parallel} + \frac{1}{m_i}\sqrt{\frac{2\Delta E}{\mu} + \left(\frac{|v_i - v_a|}{\mu}\right)^2},$$
$$u_a^{\parallel} = v_{cm}^{\parallel} - \frac{1}{m_a}\sqrt{\frac{2\Delta E}{\mu} + \left(\frac{|v_i - v_a|}{\mu}\right)^2}. \tag{15}$$

where $\Delta E = hB\times 3.5$ MHz, h is Planck's constant, $v_{cm}^{\parallel}$ in the centre-of-mass velocity parallel to the collision axis and 3.5 MHz G^{-1} is the Zeeman-energy gap in an SE transition when the ion and atom are in the electronic ground state.

Calculating the effective SE in presence of EMM. An EMM induced by a constant field can be introduced into the simulation by an additional acceleration term:

$$\ddot{\mathbf{x}} = \frac{e\mathbf{E}^{d.c.}}{m_i}, \tag{16}$$

where e is the electron charge. Only radial EMM is assumed, divided equally between the radial modes. For EMM temperature T_{EMM} in the jth mode, the electric field is

$$E_j^{d.c.} = 2\sqrt{\frac{4T_{EMM}}{m_i\Omega^2}}\frac{m_i\omega_j^2}{q_j e}. \tag{17}$$

We then numerically calculate the probability density function of the number of short-range collisions n for a given E_{EMM}, that

is, $p(n, E_{EMM})$. This probability is calculated from 10^4 trajectories for each E_{EMM} value. In the case of exothermic transition in the presence of a large enough magnetic field, we can assume that an SE event happens at most one time. The effective SE probability per Langevin collision is given by

$$p_{SE}^{eff}(E_{EMM}; p_{SE}^0) = \sum_{n=1}^{\infty} p(n, E_{EMM})(1-p_{SE}^0)^{n-1} p_{SE}^0. \quad (18)$$

From this result, we calculate the amplification factor p_{SE}^{eff}/p_{SE}^0 (Extended Data Fig. 6) for different values of EMM energy and short-range SE.

Since the probability for a collision in a single passage $p_L^{lattice}$ is less than one, and there are contributions from hot collisions with probability p_L^{bg}, the effective observed probability from the simulation is given by

$$p_{SE}^{pass}(E_{EMM}; p_{SE}^0) = p_L^{lattice} p_{SE}^{eff} + p_L^{bg} p_{SE}^0. \quad (19)$$

Using maximum likelihood estimation, we find the p_{SE}^0 value that maximizes the likelihood function.

Although the EMM is compensated throughout the experiment, the measured data are not centred around the zero voltage on the compensation electrode. Therefore, the centre of the curve was found before finding the short-range p_{SE}^0. The centre was found by a parabola fit to p_{SE}^{pass} as a function of ΔV_{comp}. The centre is shifted by 0.2073 V on the compensation electrode, corresponding to 50 μK.

Since the EMM can be coupled to the secular motion in a collision, it can heat up the ion. This effect is modelled by finding the energy distribution of the ion after a collision in the presence of specific EMM and then calculating the shelving probability P_D (ref. 47), with the parameters of the electrode that were used in this experiment. In the experiment, two shelving pulses are applied, and therefore, the double shelving probability is $P_{DS} = P_D(2 - P_D)$. Here P_{DS} as a function of EMM energy for an exothermic transition at 16 G is shown in Extended Data Fig. 7. This SE probability from the simulation results is multiplied by the corresponding shelving efficiency and presented (Fig. 2).

A simplified model for the bound state

In this section, we describe a simple model for the bound state that describes the amplification of the observed exothermic SE probability in two regimes: zero and infinite magnetic fields. We use this model to get an estimation for the mean number of short-range collisions and the lifetime of the bound state directly from the experiment, without a full calculation of the trajectories of the particles, in contrast to the MD simulation.

Assume that a bound state consists of n short-range collisions, where n has a geometric distribution with probability $p = 1/\langle N\rangle$. For each short-range collision, the SE probability p_{SE}^0 is constant.

If there is no magnetic field, the short-range SE events are independent. Therefore, for a given n, the number of SE events n_{SE} has a binomial distribution. In the experiment, only an odd number of SE events are detected, and therefore, the effective measured SE probability is given by

$$p_{SE}^{eff}(B=0) = \sum_{n=1}^{\infty} (1-p)^{n-1} p \sum_{n_{SE}\,\mathrm{odd}}^{n} B\left(n_{SE}; n, p_{SE}^0\right), \quad (20)$$

where

$$B\left(n_{SE}; n, p_{SE}^0\right) = \binom{n}{n_{SE}} \left(p_{SE}^0\right)^{n_{SE}} (1-p_{SE}^0)^{n-n_{SE}} \quad (21)$$

is the binomial distribution. On the other hand, if the magnetic field is larger than the binding energy, only one exothermic SE event is allowed. In this case, the effective probability is

$$p_{SE}^{eff}(B\to\infty) = \sum_{n=1}^{\infty} (1-p)^{n-1} p \sum_{m=1}^{n} (1-p_{SE}^0))^{m-1} p_{SE}^0. \quad (22)$$

Then, we can calculate the the ratio $p_{SE}^{eff}(B=0)/p_{SE}^{eff}(B\to\infty)$ for any N and p (Extended Data Fig. 2). From the probability of exothermic SE as a function of the magnetic field (Fig. 3), we can find the ratio $p_{SE}^{eff}(B=0)/p_{SE}^{eff}(B\to\infty) = 1.46(5)$ (Extended Data Fig. 2, red-shaded region). On the other hand, the short-range SE probability was found in the fit to the exothermic data (Fig. 2, blue line). From crossing these two curves, we can estimate the mean number of short-range collisions, $\langle N\rangle^{exp} = 8(2)$. This value is similar to the value calculated by the full MD simulation at zero magnetic field, namely, $\langle N\rangle^{MD} \approx 5.6(2)$ (Extended Data Fig. 8).

Evidently, both results give $p_{SE}^0\langle N\rangle \approx 1$. If the number of short-range collisions was larger than the exchange probability, that is, $p_{SE}^0\langle N\rangle \gg 1$, we would expect the exothermic SE rate to saturate at the Langevin rate at high magnetic fields and to approach half of the Langevin rate at low fields.

We estimate the time between subsequent collisions by solving the one-dimensional motion in the relative frame of reference. The Hamiltonian of the relative motion for a free atom–ion pair is

$$H = \frac{1}{2}\mu\dot{r}^2 - \frac{C_4}{2r^4}, \quad (23)$$

where r is the relative atom–ion separation, μ is the reduced mass and C_4 is the constant of the interaction. Assume that the initial energy of the system is negative ($-E_0 = -\frac{C_4}{2r_{max}^4}$), that is, the particles are bound with the maximum distance r_{max}. This energy is a constant of motion and we can express the velocity as a function of position as

$$\dot{r} = \frac{\mathrm{d}r}{\mathrm{d}t} = \sqrt{\frac{1}{\mu}}\sqrt{\frac{C_4}{r^4} - 2E_0}. \quad (24)$$

By integrating this equation, we can express the time of falling from a distance r_{max} to the origin by

$$t = \sqrt{\frac{\mu}{C_4}} \int_{r_{max}}^{0} \frac{r^2\mathrm{d}r}{\sqrt{1-\frac{2E_0 r^4}{C_4}}}. \quad (25)$$

The integral is analytically solvable and gives

$$t = \sqrt{\frac{\mu}{9C_4}} \frac{\sqrt{\pi}\Gamma\left(\frac{7}{4}\right)}{\Gamma\left(\frac{5}{4}\right)} r_{max}^3 \approx 1.8\sqrt{\frac{\mu}{9C_4}} r_{max}^3, \quad (26)$$

where $\Gamma(x)$ is the gamma function.

Assuming the binding is only due to the $C_4/2r^4$ potential, we can estimate the maximal distance between the particles as $r_{max} = \sqrt[4]{C_4/2E_{bind}} = 27$ nm. The falling time of two free particles in $C_4/2r^4$ potential can be analytically calculated for the one-dimensional problem, and is given by $t \approx 1.8\sqrt{\frac{\mu}{9C_4}} r_{max}^3$, which gives a falling time of $t = 31$ ns. Therefore, the period of oscillation is $T = 62$ ns, and we can estimate the lifetime of the molecule in the experiment as 0.5(1) μs.

Data availability

Source data are provided with this paper. Other data that support the findings of this study are available from the corresponding authors on a reasonable request.

References

51. Zipkes, C., Ratschbacher, L., Sias, C. & Kohl, M. Kinetics of a single trapped ion in an ultracold buffer gas. *New J. Phys.* **13**, 053020 (2011).

52. Pinkas, M. et al. Effect of ion-trap parameters on energy distributions of ultra-cold atom-ion mixtures. *New J. Phys.* **22**, 013047 (2020).
53. Meir, Ziv et al. Experimental apparatus for overlapping a ground-state cooled ion with ultracold atoms. *J. Mod. Opt.* **65**, 501–519 (2017).
54. Meir, Z. *Dynamics of a Single, Ground-State Cooled and Trapped Ion Colliding with Ultracold Atoms: A Micromotion Tale*. PhD thesis, Weizmann Institute of Science (2016).

Acknowledgements
This work was supported by the Israeli Science Foundation and the Goldring Family Foundation.

Author contributions
All authors contributed to the experimental design, construction, discussions and wrote the manuscript. M.P. collected the data and analysed the results. M.P. and O.K. wrote the numerical simulations.

Competing interests
The authors declare no competing interests.

Additional information
Extended data is available for this paper at https://doi.org/10.1038/s41567-023-02158-5.

Supplementary information The online version contains supplementary material available at https://doi.org/10.1038/s41567-023-02158-5.

Correspondence and requests for materials should be addressed to Meirav Pinkas or Roee Ozeri.

Peer review information *Nature Physics* thanks the anonymous reviewers for their contribution to the peer review of this work.

https://doi.org/10.1038/s41567-023-02158-5

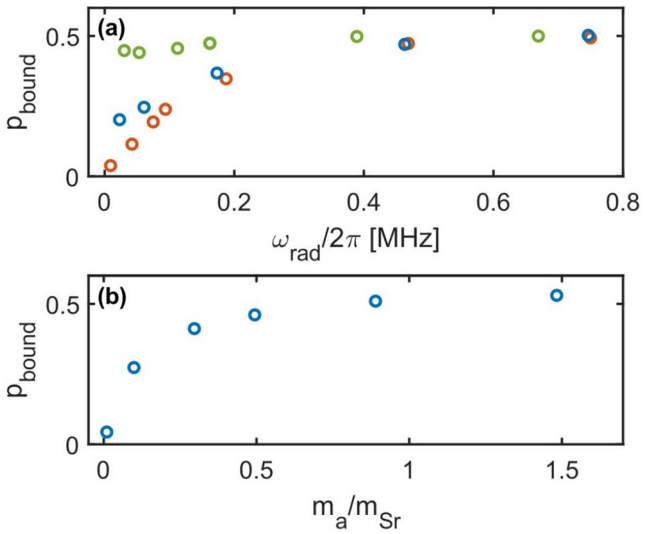

Extended Data Fig. 1 | Bound state probability in a Paul trap for different axial frequencies and atom's mass. (a) Bound state probability as a function of radial trap frequency for axial frequency of $\omega_{ax}/2\pi = 3, 100, 480$ kHz (red, blue, and green, respectively). The 3 kHz graph is the same as in Fig. 4. (b) Bound state probability as a function of the atom's mass. All parameters, apart from the atom's mass, are taken as in the experiment. The mass of the atom is changed without changing the polarization constant, C_4. For both graphs, each point corresponds to 10^4 trajectories. Confidence bounds of 1σ are on the order of marker size.

https://doi.org/10.1038/s41567-023-02158-5

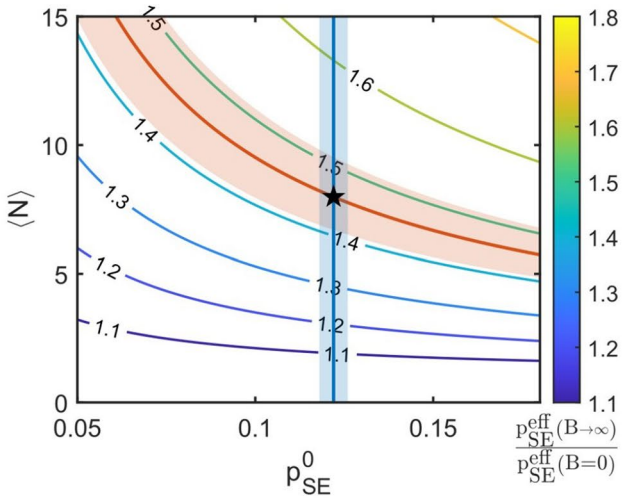

Extended Data Fig. 2 | Estimating the lifetime of bound state from the simple model. Contour lines are exothermic spin-exchange amplification, $p^{eff}_{SE}(B \to \infty)/p^{eff}_{SE}(B = 0)$, calculated by the simple bound state model, for different mean number of short-range collisions, $\langle N \rangle$, and short-range spin-exchange probability, p^0_{SE}. Red and blue bold lines are the measured ratios and short-range spin-exchange probability, respectively, with 1σ confidence bound in shaded area. The star is indicating the mean number of short-range collisions, $\langle N \rangle^{exp} = 8(2)$.

https://doi.org/10.1038/s41567-023-02158-5

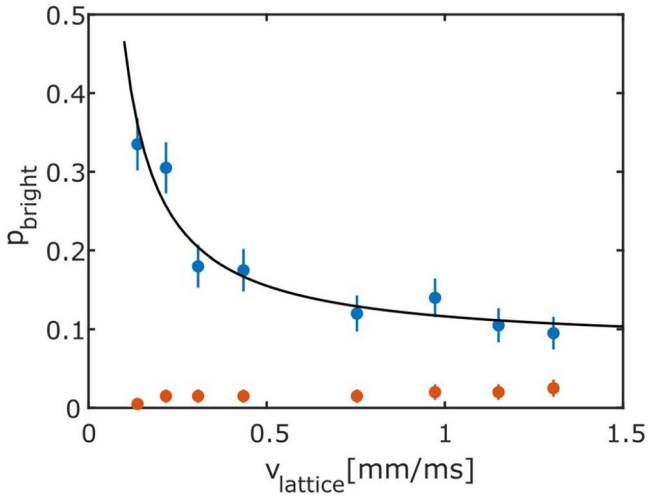

Extended Data Fig. 3 | Calibration of the number of Langevin collisions. The probability of observing the ion in a bright state after double shelving pulses with atoms (blue) and without (red) for different optical lattice velocities. When atoms are present, this probability is proportional to the probability of at least one Langevin collision in a lattice passage. Solid line is a fit to Eq. (4), with $\rho K_L = 0.039(3)$ and $p_{bg} = 0.078(8)$. Error bars are binomial distribution standard deviation.

https://doi.org/10.1038/s41567-023-02158-5

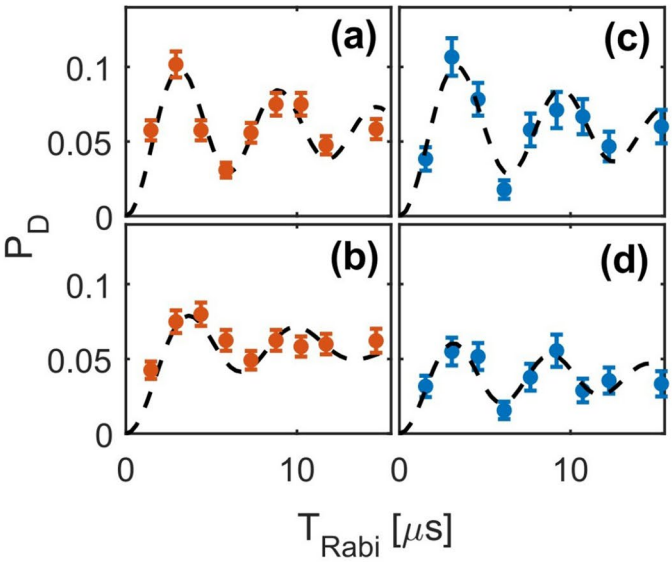

Extended Data Fig. 4 | Rabi carrier thermometry after post-selecting SE events. (a-b) Exothermic transitions at 3 G (a) and 20 G (b). (c-d) endothermic transitions at 3 G (c) and 20 G (d). Temperatures and contrast of the Rabi oscillation are written in Extended Data Table 1. Error bars are 1σ binomial standard deviation.

https://doi.org/10.1038/s41567-023-02158-5

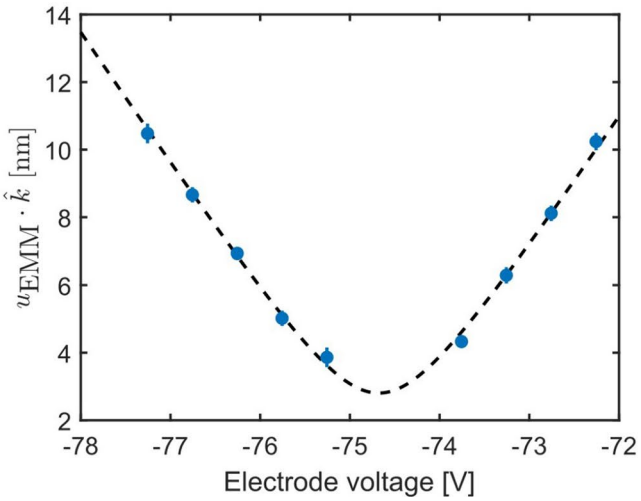

Extended Data Fig. 5 | Calibration of the EMM amplitude projection along the shelving beam axis as a function of the applied voltage on an external electrode. Measured data (blue circles) is extracted from Eq. (12) and dashed line are a fit to Eq. (13), where $\gamma_{\mathrm{proj}} = 3.97(6)$ nm/V, $V_0 = -74.68(2)$ V, and $c = 2.8(2)$ nm with 1σ confidence bounds.

https://doi.org/10.1038/s41567-023-02158-5

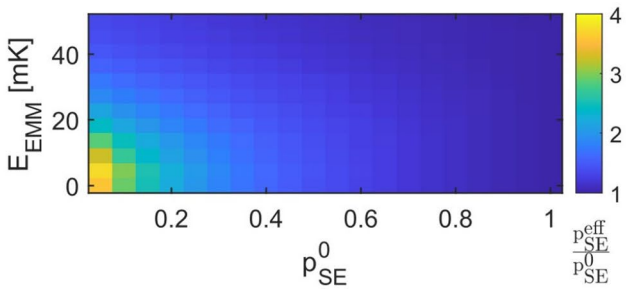

Extended Data Fig. 6 | Amplification of the short-range spin exchange, based on the MD simulation. The amplification, p_{SE}^{eff}/p_{SE}^{0}, is calculated by Eq. (18) for different EMM energies, E_{EMM}, and short-range spin-exchange probabilities, p_{SE}^{0}, at zero magnetic field.

https://doi.org/10.1038/s41567-023-02158-5

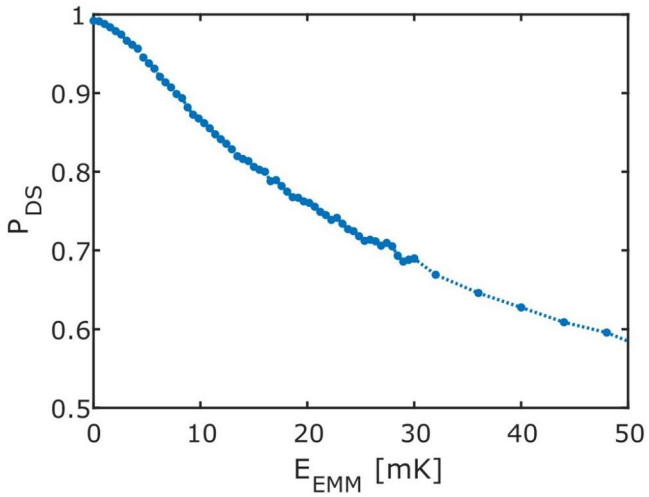

Extended Data Fig. 7 | Double shelving (DS) efficiency after a collision in presence of EMM. For each EMM energy, the shelving probability is calculated by averaging 10^4 single collision events. Exothermic reaction releasing 2.7 mK (corresponding to the energy gap at 16 G), happens after each collision.

https://doi.org/10.1038/s41567-023-02158-5

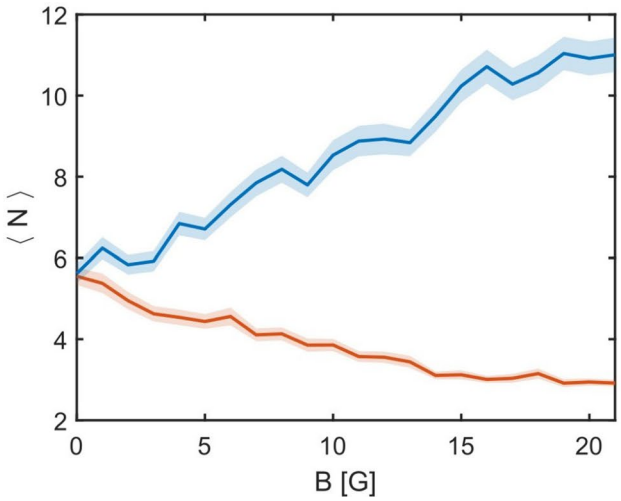

Extended Data Fig. 8 | Mean number of short-range collisions in a bound state as a function of the magnetic field as calculated by the MD simulation. The mean number of collisions is calculated for the endothermic (blue), and exothermic (red) transitions, given short-range spin-exchange probability of $p_{SE}^{0} = 0.12$. Error bars are one standard deviation calculated by bootstrapping the data-set 10 times its size.

https://doi.org/10.1038/s41567-023-02158-5

Extended Data Table 1 | Thermometry measurements

Channel	B [G]	T (atoms) [mK]	Contrast (atoms)	T (bg) [mK]	Contrast (bg)
Exothermic	3	1.3(5)	11.4(4)	0.24(3)	0.98(2)
Exothermic	20	4.4(4)	12.3(5)	0.41(5)	0.97(2)
Endothermic	3	1.2(2)	11.4(6)	0.21(2)	0.99(2)
Endothermic	20	1.5(4)	7.4(5)	0.24(4)	0.96(2)

Temperatures and contrasts fitted to Rabi cycles for different spin-exchange channels with the corresponding temperature and contrast measured on the same transition without atoms.